THE JOURNAL OF PHYSICAL CHEMISTRY C
A JOURNAL OF THE AMERICAN CHEMICAL SOCIETY

pubs.acs.org/JPCC

Article

Chemical Potential Driven Reorganization of Anions between Stern and Diffuse Layers at the Air/Water Interface

Raju R. Kumal, Srikanth Nayak, Wei Bu, and Ahmet Uysal*

Cite This: J. Phys. Chem. C 2022, 126, 1140−1151

Read Online

ACCESS | Metrics & More | Article Recommendations | Supporting Information

ABSTRACT: Ion adsorption and transfer at charged interfaces play key roles in various industrial and environmental processes. Molecular scale details of ion−ion, ion−water, and ion−surface interactions are still debated. Complex ions, such as SCN^- and $SeCN^-$, are particularly interesting due to their unexpected adsorption trends. Here, we combine vibrational sum frequency generation (VSFG) spectroscopy and surface-sensitive synchrotron X-ray studies to provide a detailed description of $SeCN^-$ adsorption at a floating charged monolayer. Polarimetry studies show that the average orientation of $SeCN^-$ anions with respect to the surface normal decreases from 45° to 22° with the increasing KSeCN concentration. Interfacial $SeCN^-$ coverage saturates at very low bulk concentrations, but their orientational organization, distribution between Stern and diffuse layers, and effects on the hydrogen-bonding network of the interfacial water continue to change with increasing bulk KSeCN concentration. These results show that the increasing chemical potential may lead to further reorganization of the adsorbed ions, even though the total interfacial ion population does not change. The reorganization of the interfacial ions and the water may be very important in chemical separations of heavy metals, where metal−anion complexes drive the selective ion transfer at aqueous interfaces.

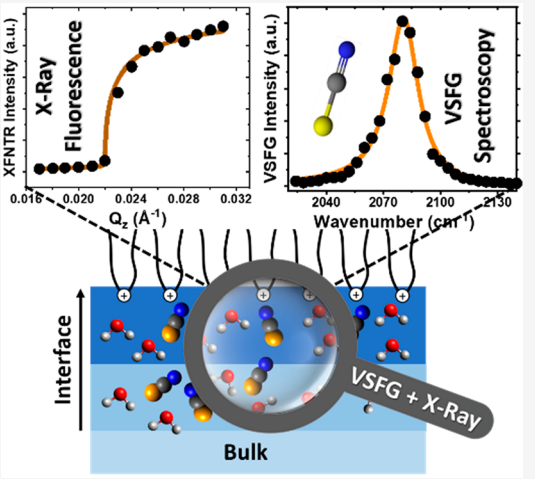

INTRODUCTION

Aqueous interfaces and how ions behave near them control many important processes, such as protein folding,[1] ice nucleation,[2,3] mineralization,[4,5] drug delivery,[6] and chemical separations.[7−13] The common point of all these processes is that the molecular scale interface significantly differs from the bulk in terms of the ion concentration, the ion speciation, and the water structure. For instance, water is layered and orientationally ordered at interfaces,[14,15] the dielectric constant is significantly lower (∼5) than the bulk value (∼80),[16,17] and the ionic species that are not present in the bulk can be stable at the interface.[18] All these differences make it difficult to predict how ions behave at interfaces based on the bulk solution properties. The difficulty increases when the ion cannot be treated as a zero-dimensional unit charge interacting with an ideal surface. Its finite size, hydration enthalpy, polarizability, and bonding properties, which are usually considered in the context of ion-specific effects, as well as the nature of the surface functional groups may lead to complex adsorption trends.[19−21]

Ion-specific effects are usually considered in an empirical framework, where ions are listed in ascending or descending order with respect to a certain effect, such as their ability to salt out proteins as described in the Hofmeister series.[19,20] It is not uncommon to see the certain ions switch positions on these empirical lists depending on the other factors in the system. In complex systems, where multiple enthalpic and entropic factors create an intricate free energy landscape, ion-specific effects may lead to qualitative differences in the ion adsorption and transfer mechanisms. For example, both nitrate (NO_3^-) and thiocyanate (SCN^-) are classified as chaotropic anions in the Hofmeister series, but they organize interfacial structure differently.[22] Adsorption of NO_3^- does not change the interfacial water structure significantly with increasing concentration while SCN^- causes significant changes, resulting in the reorganization of the interfacial water. These nanoscale differences become very important in complex processes, such as chemical separations. For instance, in liquid−liquid extraction (LLE) of the rare earth metals, the extraction trends for heavy or light lanthanides are completely reversed in the presence of nitrate or thiocyanate.[23]

Thiocyanate is one of the most studied pseudohalides because of its unique interfacial properties and its applications in separation science and electrochemistry. It is a highly

Received: August 4, 2021
Revised: December 17, 2021
Published: January 6, 2022

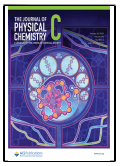

surface-active species with significant dipole moment (μ_{R-SCN} = 2.99 D),[24] which most likely navigates the ion to favorable orientation at interfaces. Recent experimental and theoretical studies have demonstrated the existence of enhanced concentration of SCN^- anions at the air/water interface even at very low bulk concentrations.[25,26] Viswanath et al. and Bian et al. showed that the average tilt angle of SCN^- anions is 45° with respect to the surface normal at the free air/water interface.[25,27−29] Saykally et al. have studied the thermodynamics of SCN^- adsorption and its charge-transfer-to-solvent spectrum at air/water interface and analyzed the solvation environments.[30,31] Selenocyanate ($SeCN^-$) has similar properties to that of SCN^- and has been used as a vibrational tag to investigate the solvent environments.[32] The strongest CN stretch frequency mode occurs at ∼2070 cm^{-1} for SCN^- and ∼2080 cm^{-1} for $SeCN^-$.[22,33] This small change is due to the slight variation in hydrogen bond strength leading to different transition dipole moments.[34,35] The dipole moment of $SeCN^-$ is reported slightly higher than that of SCN^- (μ_{R-SeCN} = 3.48 D).[24] A number of interfacial studies show that both SCN^- and $SeCN^-$ are Stark-active molecule because the CN stretch vibrational frequency is sensitive to the local environment.[36−38] Most of these studies are focused on investigation of the local structures and dynamics of anions at aqueous interfaces, but there are several unanswered questions that have yet to be addressed such as interfacial hydration and organization of ions in LLE.

It is important to understand the impact of ion-specific effects in complex chemical processes, such as LLE of heavy and precious metals. In LLE, metal ions are selectively transferred from an aqueous matrix into an organic phase with the help of amphiphilic molecules (also called extractants).[39] Because LLE is free energy driven at ambient conditions, it is relatively less energy intensive compared to other separation methods, such as distillation. The background anions in the aqueous phase have a significant impact on the extraction efficiency and selectivity. For example, heavy and light lanthanides are extracted better from SCN^- and NO_3^- solutions, respectively, when the quaternary amine methyltrioctylammonium (TOMA) is the extractant.[40] Multiple factors, such as aqueous speciation of ions, interfacial interactions, nature of the diluent, and extractant−ion complexes formed in the organic phase, are generally responsible for the selective transfer of the metal ions from an aqueous to an organic phase.[23,41]

In separation science, it is well-known that the interfacial region can affect the mass transfer and partitioning.[42,43] However, it is poorly characterized due to the experimental inaccessibility of the interface in a real extraction system. Therefore, model interfacial systems consisting of air/liquid or liquid/liquid interfaces are used to understand the interfacial interactions between extractants and ions. In general, model systems having a Langmuir monolayer have been very effective to study the interfacial water structure,[44,45] interaction of cations with monolayer,[46,47] phase transfer of metal ions,[11] and water hydrogen bond rearrangement dynamics.[9,48] With the advent of surface specific techniques such as vibrational sum-frequency generation (VSFG) spectroscopy, second harmonic generation (SHG) spectroscopy, and synchrotron X-ray scattering measurements, it has become possible to differentiate the interfacial phenomena from the bulk and study the structure and the dynamics of interfaces at the molecular level.[49−54]

VSFG and X-ray scattering are sensitive to different aspects of the interface. Therefore, their combination provides a significantly better understanding that cannot be obtained from one of them alone.[9,22,55,56] For instance, VSFG signal intensity from the −CN stretch is a combination of the number density and the orientational ordering of the $SeCN^-$ ions. X-ray fluorescence near total reflection (XFNTR) provides the interfacial number density directly. Combining these two techniques allows decoupling the contributions from the orientational ordering and the number density in VSFG experiments.

We use a monolayer of $DPTAP^+$ to model the commonly used industrial extractant quaternary ammonium $TOMA^+$. $DPTAP^+$ forms a stable monolayer at the air/aqueous interface due to its longer hydrophobic carbon chain. It has been extensively studied to investigate the adsorption of ions at charged interfaces.[22,56−60] The schematic representation of air/aqueous interface with $DPTAP^+$ monolayer, in the presence of $SeCN^-$ anions in the subphase, is shown in Figure 1. Tunable

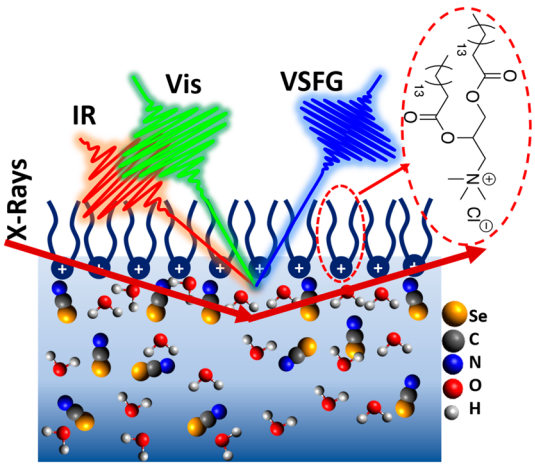

Figure 1. Schematic describing the VSFG and synchrotron X-ray experiments at the air/aqueous interface. The inset shows the structure of the $DPTAP^+$ surfactant.

IR and fixed visible beams are overlapped spatially and temporally to generate the VSFG signal from the interface. Under the electric dipole approximation, a second-order nonlinear optical process is forbidden in the bulk media having inversion symmetry, and the VSFG signal originates purely from the interfacial region.[61] The incoming X-ray beam is used to generate XFNTR and XR signals from the interface.

XFNTR is used to quantify the amount of $SeCN^-$ anions adsorbed to a charged $DPTAP^+$ monolayer at the air/aqueous interface. The incoming beam of X-rays does not penetrate into the bulk phase at small incidence angles due to total external reflection and only excites the interfacial ions.[4,62,63] This is a highly surface-sensitive technique which can quantify the elemental composition at the interface depending on the element's X-ray absorption energy. In XFNTR, the incident beam is directed to the interface slightly below and above the critical angle, and the collected fluorescence signal is plotted as a function of the incidence angle. Below the critical angle, only the interfacial ions contribute to the fluorescence signal.[64,65] Above the critical angle, both interfacial and bulk ions contribute to the signal.

https://doi.org/10.1021/acs.jpcc.1c06925
J. Phys. Chem. C 2022, 126, 1140−1151

Here, we combine VSFG, XFNTR, and XR measurements to investigate the $SeCN^-$ adsorption at the $DPTAP^+$ monolayer at the air/water interface. $SeCN^-$ is used because the Se K-edge (12.66 keV) is more convenient than the S K-edge (2.47 keV) for the XFNTR experiments. A comparison of XFNTR data to the VSFG signal from the −CN stretch under the same conditions showed that the $SeCN^-$ ions reorganize at the interface even after their interfacial number density is saturated as a function of the bulk concentration. VSFG studies of the −OH stretch of the water molecules and XR experiments support this interpretation and further elucidate that the reorganization is mainly due to the increasing $SeCN^-$ population in the Stern layer at the expense of their decreasing population in the diffuse layer.

EXPERIMENTAL METHODS

Sample Preparation. The chloride salt of DPTAP was purchased from Avanti Polar Lipids and stored at −20 °C. Potassium selenocyanate (KSeCN, ≥98%) and HPLC grade chloroform ($CHCl_3$, ≥99.9%) were purchased from Sigma-Aldrich. All glassware and sample cell used for the experiment were cleaned by soaking in a solution of Nochromix (GODAX Laboratories, Inc.) in a concentrated sulfuric acid bath for 24 h and rinsed with ultrapure water (18.2 MΩ·cm).

For the preparation of the Langmuir monolayer, a 0.25 mM DPTAP solution was made in chloroform and stored at −20 °C temperature. A circular polytetrafluoroethylene (PTFE) dish with 6 cm diameter was used as a sample cell for the VSFG experiment. A 0.25 mM DPTAP solution was added dropwise by using a 1 μL syringe (Hamilton, USA) in a sample cell containing 25 mL of subphase solution. A NIMA pressure sensor, with a chromatography paper as a Wilhelmy plate, was used to measure the surface pressure. All experiments were performed at a surface pressure of 10 mN/m at room temperature.

VSFG Experiment. The VSFG measurements are acquired by using an EKSPLA system, which has been described previously.[9,22,66] Briefly, the setup consists of a picosecond laser system, a harmonic unit, an optical parametric generator with difference frequency generation, a spectrometer, and a photomultiplier tube detector connected to a monochromator. An amplified Nd:YAG laser system produces 29 ps pulses having 28 mJ energy centered at 1064 nm with a repetition rate of 50 Hz. The harmonic unit splits the 1064 nm laser, and a portion is passed through a second harmonic crystal to generate two beams of 532 nm. One of the 532 nm beams and the 1064 nm beam are used to generate a narrow-band IR pulse tunable from 1000 to 4000 cm^{-1} via optical parametric generator and difference frequency generation. The other 532 nm laser beam which passes through an adjustable delay stage is overlapped spatially and temporarily with the IR beam to generate the sum frequency (SF) signal. The polarization of 532 nm is adjusted with a $\lambda/2$ waveplate, and the IR polarization is adjusted by using computer-controlled motorized mirrors. The SFG signal polarization is selected by using a Glan polarizer. The SFG signal is then directed to a monochromator and collected with a photomultiplier tube.

The VSFG spectrometer employs reflection geometry where the incident angles of the visible and IR beams are 60° and 55°, respectively, to the surface normal. The visible light is attenuated to an average energy of 600 μJ, and the IR energy is maintained at 100 μJ for all measurements. A motorized piezoelectric rotation stage is used to rotate the sample to avoid beam damage while probing the OH stretch region. Each spectrum is collected with a 4 cm^{-1} increment over the ranges of 2000−2200 and 2800−3800 cm^{-1} and averaged over 300 laser shots per point. The spectra are collected under various polarization combinations and are normalized against the SFG spectrum of z-cut quartz.

Theory of VSFG Spectroscopy. Vibrational sum-frequency generation (VSFG) is a second-order nonlinear spectroscopic process which is widely used for the investigation of interfacial molecular structure and dynamics. In VSFG, two input visible and IR laser beams at frequencies ω_{vis} and ω_{IR} overlap spatially and temporally on a sample surface to generate a sum frequency ($\omega_{SF} = \omega_{vis} + \omega_{IR}$) signal. The second-order nonlinear optical process is forbidden in the centrosymmetric media and thus eliminates the contributions from bulk phase.[54,67,68] The intensity of the VSFG signal (I_{SF}) is proportional to the product of the intensities of the incident beams and the square of the effective second-order nonlinear susceptibility ($\chi^{(2)}_{eff}$) of the material interface. This can be expressed as[69−72]

$$I_{SF} = \frac{8\pi^3 {\omega_{SF}}^2 \sec^2\beta}{c^3 n_1(\omega_{SF}) n_1(\omega_{vis}) n_1(\omega_{IR})} |\chi^{(2)}_{eff}|^2 I_{vis} I_{IR} \quad (1)$$

where β is the reflection angle of the sum frequency field and n_1 is the refractive index of corresponding medium. There are 27 components of $\chi^{(2)}$, but in the case of azimuthally isotropic interface, there are only four independent nonvanishing components: $\chi_{xxz} = \chi_{yyz}$, $\chi_{zxx} = \chi_{zyy}$, $\chi_{xzx} = \chi_{yzy}$, and χ_{zzz}, where z is defined to be the direction normal to the surface. These four components can be deduced by measuring VSFG at different polarizations: SSP, SPS, PSS, and PPP (SF, visible, and IR fields, respectively). The $\chi^{(2)}_{eff}$ consists of nonresonant ($\chi^{(2)}_{NR}$) and resonant ($\chi^{(2)}_{R}$) terms. The VSFG intensity is enhanced when the frequency of incidence IR beam is on resonance with a vibrational mode of an interfacial molecule.

$$|\chi^{(2)}_{eff}|^2 \propto \left| \chi^{(2)}_{NR} + \sum_{\nu} \frac{A_\nu}{\omega_{IR} - \omega_\nu + i\Gamma_\nu} \right|^2 \quad (2)$$

where A_ν is resonance amplitude, ω_ν is the resonant frequency, and Γ_ν is the damping constant of νth vibrational mode which describes the line width of the transition.

For a charged interface, in addition to the $\chi^{(2)}_{R}$ there is also the $\chi^{(3)}$ contribution to the SFG signal which originates due to the static electric field that aligns the bulk molecules.[73−79]

$$|\chi^{(2)}_{eff}|^2 \propto \left| \chi^{(2)}_{NR} + \sum_{\upsilon=1}^{n} \chi^{(2)}_{R} e^{i\gamma_\upsilon} + \frac{\kappa}{\sqrt{\kappa^2 + (\Delta k_z)^2}} e^{i\varphi} \chi^{(3)} \Phi(0) \right|^2 \quad (3)$$

where $\chi^{(3)}$ is the third-order nonlinear susceptibility, γ_ν is the $\chi^{(2)}_{R}$ phase angle, κ is the inverse of the Debye screening length, Δk_z is the inverse of the coherence length of the SFG process, φ is the $\chi^{(3)}$ phase angle, and $\Phi(0)$ is the surface potential. The additional detail and the fitting Mathematica code can be accessed in the work published by Ohno et al.[73] The $\chi^{(2)}_{eff}$ term gives information about the number density and orientation and can also be expressed in the following form:

$$\chi^{(2)}_{eff} = N_s d(\langle \cos\theta \rangle - c\langle \cos^3\theta \rangle) = N_s d r(\theta) \quad (4)$$

https://doi.org/10.1021/acs.jpcc.1c06925
J. Phys. Chem. C 2022, 126, 1140−1151

where N_s is effective surface number density, $r(\theta)$ is orientational distribution, θ is the molecular orientation angle to the surface normal, d is the susceptibility strength factor proportional to the hyperpolarizability value, and c is the general orientational parameter.

Synchrotron X-ray Experiments. XFNTR and XR are used for the investigation of interfacial population and organization of ions at air/aqueous interface. XR and XFNTR measurements were performed by using a Langmuir trough integrated with a synchrotron X-ray beamline at sector 15-ID-C, NSF's ChemMatCARS of the Advanced Photon Source at Argonne National Laboratory. The X-ray energy was 17.3 keV, and all experiments were conducted at room temperature. The Langmuir trough was enclosed in a gastight chamber and was purged with helium to reduce the beam damage and the background scattering. The XR signal was recorded by a Pilatus 100 K area detector, and the XFNTR signal was recorded by a Votex-60 EX multicathode energy-dispersive X-ray detector placed 10 mm above from the sample surface. A brief description of XFNTR data analysis is given in the Supporting Information.

The XR data were measured as a function of the wave vector transfer, $\overrightarrow{Q_z} = (4\pi/\lambda)\sin\alpha$, by varying the incidence angle (α). For 17.3 keV energy, the wavelength (λ) of the X-ray beam is 0.72 Å. The DPTAP monolayer is modeled by two slabs for the 2.5 μM and 25 mM samples, with one slab corresponding to the hydrophobic tail group and other for the hydrophilic headgroup plus the adsorbed ions. The intermediate concentration, 2.5 mM, sample required a three-box model. The thickness, electron density, and the roughness of the layers are determined by fitting the experimental data using a Parratt algorithm.[62,65,80] The X-ray energy of 17.3 keV used for the XFNTR measurement was above the K absorption edge of Se (12.66 keV).

RESULTS AND DISCUSSION

Figure 2a–e shows the variation of XFNTR intensity as a function of the vertical momentum transfer (Q_z) for $SeCN^-$ adsorption at DPTAP monolayer at various bulk KSeCN concentrations. A similar measurement from a 25 mM KSeCN solution without a monolayer was used for calibration (Figure S1). The solid lines are the best fits to the experimental data. The fits use a model that considers the geometry of the experimental setup and the X-ray absorption and emission energies.[4,81] In the presence of the monolayer, the intensity of XFNTR signal increases linearly with the increasing Q_z below the critical angle (Q_c = 0.022 $Å^{-1}$), indicating the anion adsorption at the interface. At low bulk concentrations, the signal intensity decreases above Q_c due to the decreasing transmission and very small bulk concentration, whereas for higher bulk concentrations, the bulk signal dominates above Q_c. The data below the critical angle are shown in Figure 2f separately to better display the changes in fluorescence intensity caused by the interfacial ion adsorption. The total number of $SeCN^-$ anions adsorbed at the interface is saturated at 0.5 mM bulk concentration, which can be observed in the raw data without fitting (Figure 2f). The fit results show that the maximum molecular area per $SeCN^-$ is ~53 ± 1 $Å^2$ (at 2.5 mM bulk concentration), which is slightly more than the area per $DPTAP^+$ molecule for high concentration samples (~43 $Å^2$), obtained from grazing incidence X-ray diffraction (GID) measurements (Figure S2),[22] suggesting that the charge

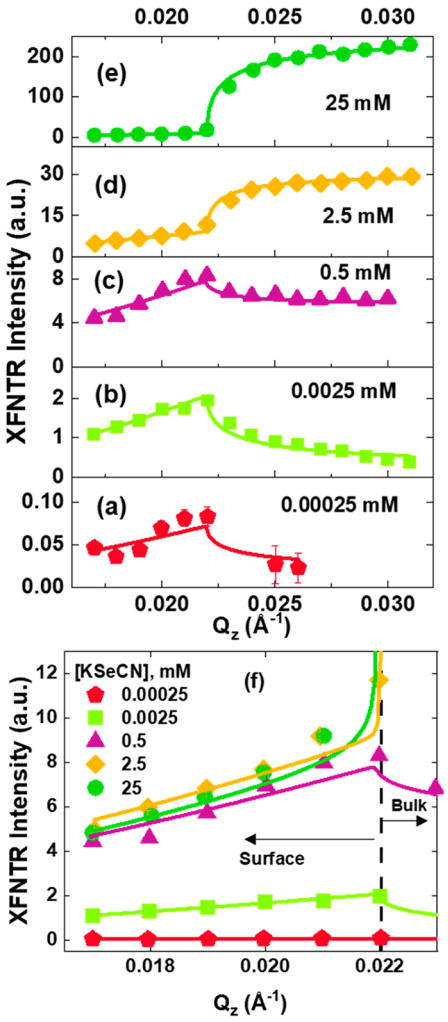

Figure 2. (a–e) XFNTR measurements at different $SeCN^-$ concentrations. The solid lines are the best fits to the experimental data. (f) Zoomed-in version of the data and fit below the critical angle (Q_c ~ 0.022 $Å^{-1}$) for all data sets in (a–e), displaying the change in XFNTR intensity due to $SeCN^-$ adsorption at the interfacial region.

neutrality is nearly satisfied between the positively charged headgroups and the adsorbed $SeCN^-$ ions. XFNTR does not distinguish between Stern and diffuse layers and provides the total number of interfacial $SeCN^-$ ions within 5–7 nm of the surface. Below, we discuss how the orientational ordering of $SeCN^-$ ions continues to change even after this overall saturation.

The vibrational signatures of the CN stretch region (2000–2200 cm^{-1}) of $SeCN^-$ ions under PPP, SSP, and SPS polarization combinations are directly probed by using VSFG spectroscopy. Figure 3a–c shows the variation of VSFG intensity as a function of IR frequency at various KSeCN concentrations under different polarization combinations. A single-peak Lorentz function (eq 3) accounting both $\chi^{(2)}$ and $\chi^{(3)}$ contributions is used to fit the experimental data under PPP and SPS polarizations, and the fit parameters are tabulated in Table S1. The signal intensity under PPP polarization is higher and monotonically increases with increasing KSeCN bulk concentration. On the other hand, the VSFG signals under SSP and SPS polarizations are found to be less sensitive to the bulk concentration. Under SSP polarization, the VSFG

https://doi.org/10.1021/acs.jpcc.1c06925
J. Phys. Chem. C 2022, 126, 1140–1151

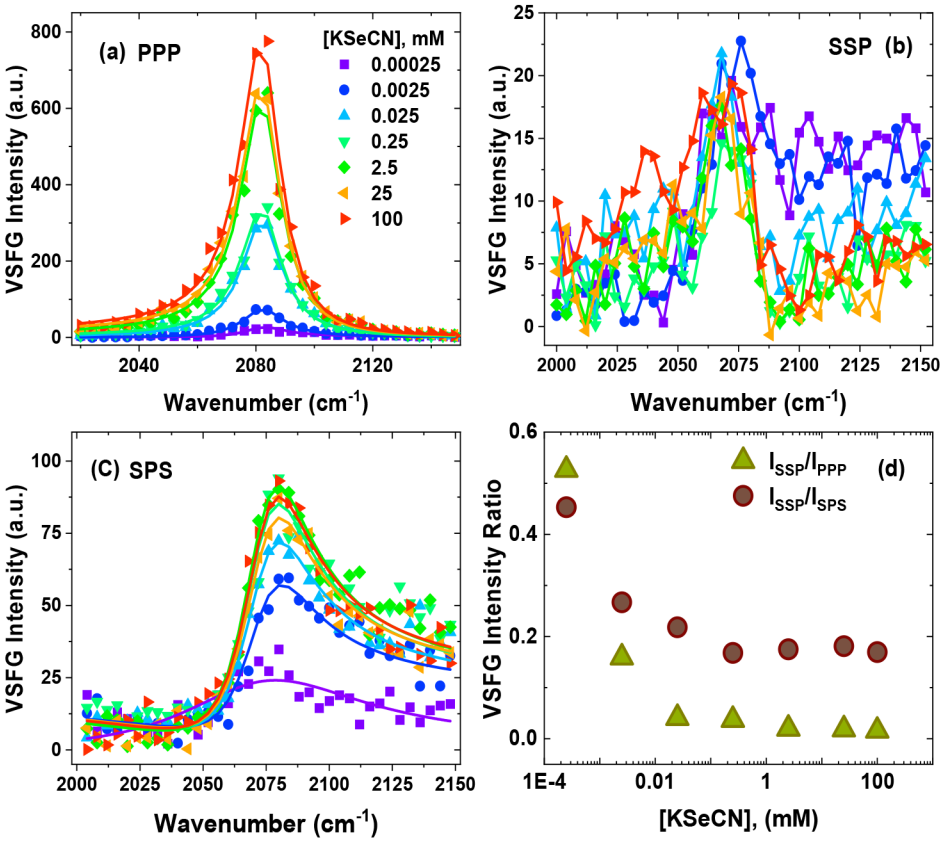

Figure 3. Variation of VSFG intensity for the CN stretch region of $SeCN^-$ ions under (a) PPP, (b) SSP, and (c) SPS polarization combinations. The solid lines in (a) and (c) are the fits to the experimental data and in (b) are the lines following the data points as visual guides. Panel d is the variation of the ratio of the VSFG intensity at a maximum amplitude obtained under different polarizations with KSeCN bulk concentration.

intensity is almost indistinguishable from the background and does not appear to increase with increasing concentration. This could be due to the interference of the small resonant feature of the CN stretch with background signal in the absence of salt in the subphase. The background signals of DPTAP/water in the absence of salt under different polarizations are given in Figure S4. The same measurement under SPS polarization results in a slightly higher intensity compared to the SSP case and appears to increase slightly for the lowest three KSeCN concentrations before plateauing at around 0.025 mM.

The relatively stronger VSFG signal under PPP polarization indicates a constructive interference between the $\chi^{(2)}$ components and $SeCN^-$ enrichment at the interface. The PPP polarization configuration probes the combination of *zzz*, *xxz*, *zzx*, and *zxx* components of $\chi^{(2)}$ while SSP and SPS selectively probes only *xxz* and *xzx* components, respectively. The intensity of the VSFG signal is the square of the product of effective number density (N_s) and the average orientation ($\langle r(\theta)\rangle$) of $SeCN^-$ anions at the interface as given by eq 4. The SSP polarization probes the vibrational modes having a component of dipole moment perpendicular to the interface, and the SPS detects those parallel to the interface.[82] The lower intensity obtained under SSP and SPS polarization suggests that the $SeCN^-$ anions have intermediate orientation. By taking the ratio of the SSP to PPP and SSP to SPS signal, it is possible to determine the actual orientation of the $SeCN^-$ anions.[25,69] The corresponding SSP to PPP signal ratio varies from 0.6 to 0.02, and the SSP to SPS signal ratio varies from 0.5 to 0.2 as the KSeCN concentration increases (Figure 3d). The calculation of the interfacial orientation of $SeCN^-$ anions is based on the assumption that the angular distribution of molecular orientation is a δ function. Our experimentally obtained ratios are compared with the simulated curve of the VSFG intensity ratio available in the literature.[25] This suggests that the average orientation of anions with respect to surface normal decreases from 45° to 22° with the increasing KSeCN concentration. At lower concentrations, anions are loosely packed and orient at a greater angle with respect to surface normal, but with the increasing concentration, they orient more parallel to the surface normal.

The results obtained from the analysis of XFNTR and the CN stretch of VSFG measurements are plotted together in Figure 4. Blue circles are the average surface coverage of $SeCN^-$ anions obtained from XFNTR fit. Stars and triangles are the VSFG fit amplitudes of the CN stretch region under PPP and SPS polarizations, respectively, as a function of bulk KSeCN concentration. A Langmuir adsorption isotherm is used to fit the $SeCN^-$ ion coverage obtained from XFNTR to display the variation. The full coverage ($1\ A_{UC}^{-1}$, where A_{UC} is the unit cell area of a DPTAP molecule) is defined as the coverage when there is one $SeCN^-$ anion per DPTAP molecule at the interface. The surface coverage plot shows that the adsorption of $SeCN^-$ ions increases with increasing bulk concentration and appears to saturate at 0.5 mM. Conversely, the area under the curve of the CN stretch region under PPP polarization does not appear to saturate. These two results together suggest that the orientational reorganization of $SeCN^-$ ions continues after their total numbers in Stern and

https://doi.org/10.1021/acs.jpcc.1c06925
J. Phys. Chem. C 2022, 126, 1140−1151

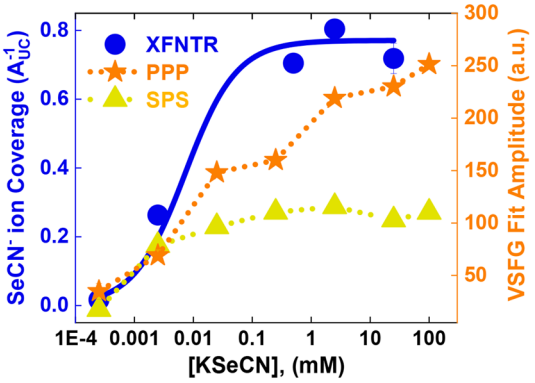

Figure 4. Variation of CN stretch VSFG fit amplitude (PPP and SPS polarizations) and the surface coverage of $SeCN^-$ ions as a function of KSeCN salt concentration obtained from XFNTR measurements. The blue solid line is the Langmuir fit to the corresponding XFNTR data set. The dotted lines are following the data points for clarity. Error bars are smaller than the symbols, except for 20 mM XFNTR data.

diffuse layers saturate. The increase in the VSFG signal under PPP combination is not exactly monotonic but appears to have some steps; that is, the intensity stays almost constant within certain bulk concentration ranges before jumping to a higher value. A similar behavior was observed with SCN^- in our previous studies.[22] The comparable values of fit amplitudes obtained for two lowest concentrations under SPS and PPP polarizations suggest that the anion orientation is not changing at very low concentrations.

We used XR to investigate the details of the interfacial reorganization after apparent saturation of the $SeCN^-$ coverage (Figure 5). XR is sensitive to the electron density gradient at the interface.[4] Therefore, $SeCN^-$ ions adsorbing in the Stern layer can be detected from their effects on the total electron density around the headgroup region of the DPTAP. However, $SeCN^-$ ions in the diffuse layer that do not form a well-defined layer have a much smaller effect on XR.[62] Because XFNTR is sensitive to all $SeCN^-$ ions in both Stern and diffuse layers and XR is mostly sensitive to the $SeCN^-$ ions in the Stern layer, their comparison will elucidate the relative distribution of $SeCN^-$ ions between these layers.

Figure 5a shows the X-ray reflectivity intensity (R) from the DPTAP monolayer on pure water, 2.5 μM, 2.5 mM, and 25 mM KSeCN concentrations normalized to the Fresnel reflectivity (R_F) from an ideally flat interface. The solid lines are the best fits to the experimental data using a box model. This model represents the interface as uniform electron density layers with error function interfaces (to account for the roughness) between them. Then, the calculated reflectivity is compared to the data, and the fit parameters, including the length, electron density, and roughness, are optimized by using a least-squares fitting method (Table S2).[83] Electron density profiles (EDPs) are plotted by using these fit parameters (Figure 5b).

The EDP of DPTAP on 2.5 μM KSeCN solution (Figure 5b) is very similar to that of on pure water which indicates a very small (or negligible) $SeCN^-$ adsorption in the Stern layer. However, XFNTR shows 0.02 A_{UC}^{-1} coverage for $SeCN^-$, which corresponds to 1 $SeCN^-$ per 50 $DPTAP^+$. Similarly, VSFG shows a small but detectable signal from $SeCN^-$ at all polarization combinations. As discussed above, the SSP/PPP and SPS/PPP intensity ratios suggest that the average angle

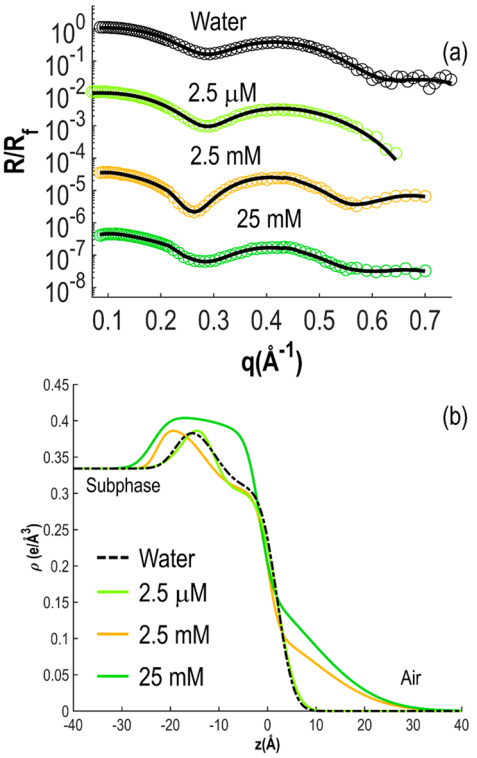

Figure 5. (a) XR data (symbols) and fit (lines) at three different bulk KSeCN concentrations and on pure water. (b) EDPs derived from the fits to the XR data in (a).

from the surface normal is around 45° at this concentration (Figure 3d), which is very similar to the orientation observed with SCN^- at the free air/water interface.[25] Therefore, it is reasonable to say that at 2.5 μM bulk concentration the $SeCN^-$ ions mostly adsorb in diffuse layer, and they do not directly interact with the DPTAP monolayer.

At 2.5 mM bulk concentration, the electron density at the headgroup region increases, suggesting some $SeCN^-$ adsorption in the Stern layer. Also, the overall roughness of the interface increases. The increase in roughness is not specific to $SeCN^-$. A similar trend was observed even with simpler anions, such as Cl^-, Br^-, and I^-.[56] According to the XFNTR, the total coverage of $SeCN^-$ is saturated at this concentration (Figures 2 and 4).

At 25 mM bulk concentration, the electron density of the headgroup region significantly increases. Considering that the total $SeCN^-$ coverage determined by XFNTR has already saturated, it is reasonable to suggest that at this concentration the ions that were already adsorbed in diffuse layer move to the Stern layer, but the total coverage does not change. This behavior is very similar to the two-step adsorption observed with $PtCl_6^{2-}$ anions in previous studies.[62,84]

The anion adsorption and its interfacial organization are further investigated by probing the OH stretch region of water under SSP polarization (Figure 6). The two peaks near 3200 and 3400 cm^{-1} are characteristics of hydrogen-bonded water molecules near the interface and are assigned to strongly and weakly hydrogen-bonded OH stretch of the water molecules, respectively.[44,85] The OH stretch region is fitted globally with two-peak Lorentz function using eq 2 to simplify the analysis. The peak positions and widths were forced to be same for all concentrations, varying only the amplitude of the resonances.

https://doi.org/10.1021/acs.jpcc.1c06925
J. Phys. Chem. C 2022, 126, 1140−1151

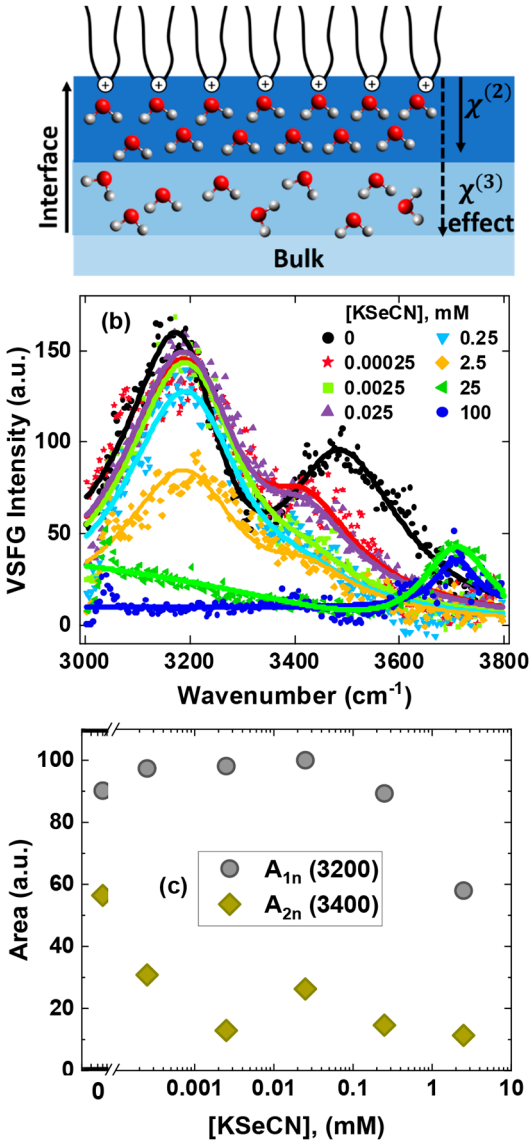

Figure 6. (a) Schematic representation of a positively charged $DPTAP^+$ interface in the absence of salt. (b) VSFG signal from the OH stretching region of water at various KSeCN concentrations under the DPTAP monolayer. The solid lines are the fit to the experimental data using two Lorentzian peaks (centered at ~3180 and ~3440 cm^{-1}) as described in the text. (c) Variation of the area under each Lorentzian peak as a function of the bulk KSeCN concentration.

The fit parameters obtained are tabulated in Table S3. The area under the curve for each Lorentz peak is calculated and plotted as a function of KSeCN concentration (Figure 6c). The area under the A_{1n} (3200 cm^{-1}) band, which originates due to a stronger H-bonding network, remains mostly unchanged until the bulk KSeCN concentration reaches 0.025 mM and then drops at higher concentration. The band completely disappears for 25 and 100 mM salt concentrations. Conversely, the area under the A_{2n} (3400 cm^{-1}) band which originates due to weaker H-bonding network sharply drops even for the lowest KSeCN concentration. With the increasing concentration, the 3400 cm^{-1} band either disappears or has very low intensity, and only the 3200 cm^{-1} band is visible. A qualitatively similar behavior was observed with SCN^- ions in our previous studies.[22] However, in that case, the 3400 cm^{-1} band disappeared at 0.025 mM bulk concentration, while it is still visible at 2.5 mM bulk concentration in this case. The overall line shape of the 3200 cm^{-1} peak was also different with SCN^-.

The charged interface induces highly ordered H-bonding networks in water molecules which relax away in a few monolayers, depending on the solution conditions.[74] The charged interface has second-order $\chi^{(2)}$ and third-order $\chi^{(3)}$ contributions to the VSFG signal. The $\chi^{(2)}$ contribution is from the interfacial molecules (primarily from the Stern layer) which are asymmetrically oriented and hence induce an electric dipole allowed VSFG signal. The static electric field of the charged interface also aligns the bulk water molecules (in the diffuse layer), which is called the $\chi^{(3)}$ effect, where $\chi^{(3)}$ is the third-order nonlinear susceptibility of water.[73,74,86−89] In the absence of salt (0 mM KSeCN), the VSFG intensity of the OH stretch region of water from the air/aqueous interface is strongly enhanced due to both $\chi^{(2)}$ and $\chi^{(3)}$ effects. This is schematically represented in Figure 6a. Addition of the salt decreases $\chi^{(2)}$ by breaking the interfacial H-bonding networks and disturbing the orientational ordering of water molecules. The $\chi^{(3)}$ effect decreases after the addition of salt due to screening of static electric field of the charged interface.

At lower KSeCN concentrations, $\chi^{(2)}$ appears unaffected, but the $\chi^{(3)}$ effect decreases due to screening of the static electric field of the charged interface experienced by the water molecules in the diffuse layer. The decrease in the intensity of the 3400 cm^{-1} band may suggest the breaking down of the weakly H-bonded water networks in the diffuse layer.[90] This band is also shifted toward lower wavenumber region (red-shift) which is an indication of increased interaction of water molecules with the surrounding ions, here $SeCN^-$.[91] The 3200 cm^{-1} band remains almost unchanged until the KSeCN bulk concentration is 0.25 mM, suggesting that the interfacial H-bonding network (or $\chi^{(2)}$) is barely affected up to this concentration, and the 3200 cm^{-1} band has major contribution from $\chi^{(2)}$. The small Stern layer adsorption determined by XR at lower KSeCN concentration supports this interpretation (Figure 5b). We hypothesize that weakly hydrogen-bonded water molecules are affected from the presence of a small number of $SeCN^-$ ions, but the strongly hydrogen-bonded water molecules are not. Similar behavior was observed by Jena and Hore et al. at a charged silica interface under varying salt concentrations.[86,92] It is known that simple anions, such as Cl^-,[56] or the anions that do not disturb the weak H-bonding network significantly, such as NO_3^-,[22] lead to a more uniform decrease in the VSFG signal mostly through the $\chi^{(3)}$ effect, without affecting the overall bimodal shape of the signal.

The 3200 cm^{-1} band decreases significantly (Figure 6c) as the concentration is increased from 0.25 to 2.5 mM KSeCN, which suggests that the ions start to move from diffuse to the Stern layer. Consequently, the $\chi^{(2)}$ effect decreases in addition to the decrease of the $\chi^{(3)}$ effect due to breaking down of the ordered interfacial H-bonding networks of water. The results obtained from the VSFG measurements of the CN stretch region under PPP polarization also show a significant increase of its intensity (Figures 3a and 4) at this concentration window, referring to the possible transfer of ions and their reorganization. On the other hand, the slightly higher electron density profile at the 2.5 mM KSeCN concentration compared to its value at the lowest concentration (Figure 5b) suggests that the most of the $SeCN^-$ ions are still in the diffuse layer.

https://doi.org/10.1021/acs.jpcc.1c06925
J. Phys. Chem. C 2022, 126, 1140−1151

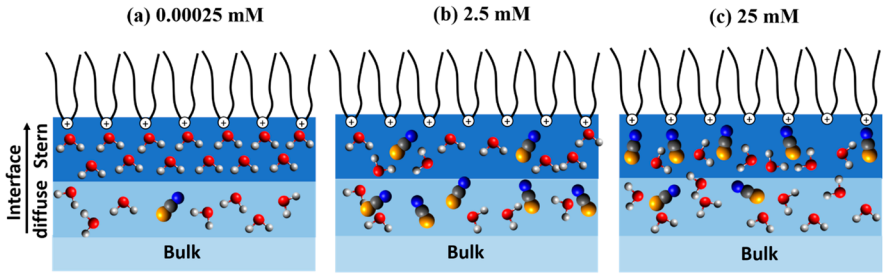

Figure 7. Schematic summarizing the results obtained from XFNTR, VSFG, and XR studies regarding the interfacial $SeCN^-$ and water organization as a function of bulk KSeCN concentration: (a) 0.00025 mM, ions are mostly in the diffuse layer; (b) 2.5 mM, ions start to move to the Stern layer but still the majority of the ions are in the diffuse layer; and (c) 25 mM KSeCN, ions are now mostly in the Stern layer.

At higher salt concentrations (≥25 mM), the H-bonding environment of water near the interface is heavily affected by the adsorption of $SeCN^-$ anions, and the OH stretch bands at 3200 and 3400 cm^{-1} disappear. At this concentration, both $\chi^{(2)}$ and $\chi^{(3)}$ effects are significantly decreased due to the displacement of ordered interfacial water network by the $SeCN^-$ anions. This agrees with the XR data which show that the electron density of the headgroup region significantly increases at 25 mM bulk concentration, indicating enhanced Stern layer adsorption. Also, a new band around 3700 cm^{-1} appears. This band is commonly observed in the case of neat air/water interface and corresponds to the non-hydrogen-bonded free OH that points toward the air. At the air/water interface, more than 20% of water molecules have free non-hydrogen-bonded OH which collectively give a sharp peak at 3700 cm^{-1}. This peak is expected to disappear in the presence of the DPTAP monolayer, as observed at lower salt concentrations (≤2.5 mM).

The reappearance of the 3700 cm^{-1} peak at higher concentrations can be due to a few reasons. One possibility is that the monolayer structure is disturbed, and some parts of the surface are open, allowing free OH bonds to stick out of the surface. However, this possibility is ruled out by investigating the CH stretch region (Figure S3). The absence of any significant gauche defect from CH_2 groups (2855 cm^{-1} band) for all concentrations indicates that the monolayer is well-packed and stable even at higher salt concentrations. Similarly, GID results show no difference between 2.5 and 25 mM samples (Figure S2). This is also supported by the monotonically increasing CN stretch intensity under PPP polarization (Figures 3a and 4), which could have decreased if the monolayer was largely disturbed. There is slight decrease in CH peak intensity (CH_3 stretching at 2875 cm^{-1} and its Fermi resonance peak at 2937 cm^{-1}) at higher concentration which is evidence of a subtle disorder in the monolayer packing, but this is unlikely to be enough to cause any open regions in the monolayer. In the presence of a stable and well-packed monolayer, it is unlikely that the reappearing 3700 cm^{-1} peak is solely a result of the dangling OH.

A second possibility is that the 3700 cm^{-1} peak originates from the water molecules coordinating to $SeCN^-$ ions. It is found that the shape and phase of dangling OH and the OH mode of water complexed with anions are similar.[90] This suggests that the 3700 cm^{-1} peak at higher concentration could be the result of $SeCN^-$:H_2O complexation at the Stern layer because both XR (Figure 5b) and VSFG (Figure S3) do not show a significant difference in the tail region between 2.5 and 25 mM samples. The broadening of this peak compared to the pure air/water interface indicates the presence of asymmetric bonding environments. Further investigations with molecular dynamics simulations can elucidate the origins of this peak as it was done in the case of the 3600 cm^{-1} peak appearing in the presence of $PtCl_6^{2-}$ and $PdCl_4^{2-}$ anions.[9,66] Nevertheless, VSFG studies of the OH stretch clearly show that the interfacial water reorganization continues above 0.1 mM bulk concentration, consistent with $SeCN^-$ reorganization identified by XR and XFNTR experiments.

Figure 7 summarizes the interpretation obtained by comparing all experimental data presented above. The change in interfacial water structure due to the adsorption of $SeCN^-$ ions as a function of KSeCN bulk concentration is demonstrated schematically by considering the three concentrations where the notable changes are observed. At very low concentration, 0.00025 mM, the majority of the $SeCN^-$ ions are in the diffuse layer. This is based on the combination of three experimental results. XFNTR and VSFG of the −CN stretch show the presence of the SeCN at the interface. However, XR does not show any significant adsorption in the Stern layer. Also, only the 3400 cm^{-1} peak in the −OH region VSFG data is affected from the adsorbed anions. The total coverage is saturated around 0.5 mM bulk concentration according to the XFNTR result, but ions further reorganize at the interface. At 25 mM, ions are significantly adsorbed at the Stern layer which continue to reorganize until 100 mM bulk concentration. These results highlight the importance of investigating the anion adsorption and the corresponding interfacial water structure for a better understanding of chemical, physical, and biological processes. We note that the estimation of the $\chi^{(3)}$ term is based on the Gouy−Chapman model of the variation of surface charge with counterion concentration.[73] This is an approximation in lieu of better analytical models to estimate the surface charge when specific ion effects play a role. Understanding the nonclassical effects of ion adsorption at charged interfaces, as in this study, would facilitate more accurate interpretations of SFG results on charged interfaces.

CONCLUSIONS

Complex anions, such as SCN^- and NO_3^-, play important roles in chemical separations and other environmental and industrial processes, yet very little is known about their interfacial effects. We have studied $SeCN^-$ adsorption at a positively charged DPTAP monolayer with multiple surface sensitive probes and identified important differences in the way they adsorb compared to the simple anions, such as Cl^- or Br^-. At very low bulk concentrations (<2.5 μM), a greater number of $SeCN^-$ anions adsorb in the diffuse layer, without a direct interaction with the DPTAP. This is in contrast to the typical

https://doi.org/10.1021/acs.jpcc.1c06925
J. Phys. Chem. C 2022, 126, 1140−1151

picture of ion adsorption at a charged interface, where the ions adsorb in the Stern layer first. At intermediate bulk concentrations (~2.5 mM), the $SeCN^-$ anion surface coverage reaches a maximum, and the anions adsorb in both diffuse and Stern layers. They mostly disturb the weakly hydrogen-bonded water molecules but do not affect the ordered hydrogen-bonded water network at the interface. At the higher bulk concentrations (>25 mM), the total $SeCN^-$ surface coverage does not increase, but the majority of the anions move to the Stern layer; their orientation becomes more parallel to the surface normal, typical water peaks (3200 and 3400 cm^{-1}) disappear, and a new water population appears creating a VSFG signal at 3700 cm^{-1}. These detailed observations were possible thanks to the complementary use of XFNTR, XR, and VSFG techniques which provided a unique sensitivity to the ions in diffuse and Stern layers as well as their orientational ordering. It is usually difficult to disentangle the effects of the number density and the orientational ordering on the VSFG signal intensity. Obtaining the number density from XFNTR independently allowed a better interpretation of −CN stretch results. Utilizing XR to determine the ion adsorption in Stern layer helped in the interpretation of the concentration-dependent changes in the CN and OH region VSFG experiments. These results clearly show that a simple quantitative list of strongly or weakly adsorbing ions (usually considered in the context of Hofmeister series) is not enough to describe the ion-specific effects of complex anions. Their interfacial adsorption behavior and effects on the hydrogen-bonding network change significantly as a function of the surface coverage, which, in turn, is expected to affect the resulting interfacial processes in the presence of these complex anions.

■ ASSOCIATED CONTENT

Supporting Information

The Supporting Information is available free of charge at https://pubs.acs.org/doi/10.1021/acs.jpcc.1c06925.

Fit parameters of the CN and OH stretch region of VSFG spectra, and XR measurements, XFNTR plot at 25 mM KSeCN bulk concentration in the absence of DPTAP monolayer, GID results, CH stretch region of DPTAP monolayer under SSP polarization in the presence of different KSeCN concentrations, and a brief description of XFNTR data analysis (PDF)

■ AUTHOR INFORMATION

Corresponding Author

Ahmet Uysal − *Chemical Sciences and Engineering Division, Argonne National Laboratory, Lemont, Illinois 60439, United States;* orcid.org/0000-0003-3278-5570; Phone: +1-630-252-9133; Email: ahmet@anl.gov

Authors

Raju R. Kumal − *Chemical Sciences and Engineering Division, Argonne National Laboratory, Lemont, Illinois 60439, United States;* orcid.org/0000-0002-6077-8741

Srikanth Nayak − *Chemical Sciences and Engineering Division, Argonne National Laboratory, Lemont, Illinois 60439, United States;* orcid.org/0000-0003-0213-5796

Wei Bu − *NSF's ChemMatCARS, The University of Chicago, Chicago, Illinois 60637, United States;* orcid.org/0000-0002-9996-3733

Complete contact information is available at: https://pubs.acs.org/10.1021/acs.jpcc.1c06925

Notes

The authors declare no competing financial interest.

■ ACKNOWLEDGMENTS

This material is based upon work supported by the U.S. Department of Energy, Office of Science, Office of Basic Energy Sciences, Separation Science program, under Contract DE-AC02-06CH11357. Use of the Advanced Photon Source, an Office of Science User Facility operated for the U.S. Department of Energy (DOE) Office of Science by Argonne National Laboratory, was supported by the U.S. DOE under Contract DE-AC02-06CH11357. NSF's ChemMatCARS Sector 15 is supported by the Divisions of Chemistry (CHE) and Materials Research (DMR), National Science Foundation, under Grant NSF/CHE-1834750.

■ REFERENCES

(1) Lo Nostro, P.; Ninham, B. W. Hofmeister phenomena: an update on ion specificity in biology. *Chem. Rev.* **2012**, *112*, 2286−2322.

(2) Lovering, K. A.; Bertram, A. K.; Chou, K. C. New Information on the Ion-Identity-Dependent Structure of Stern Layer Revealed by Sum Frequency Generation Vibrational Spectroscopy. *J. Phys. Chem. C* **2016**, *120* (32), 18099−18104.

(3) Nagata, Y.; Hama, T.; Backus, E. H.; Mezger, M.; Bonn, D.; Bonn, M.; Sazaki, G. The surface of ice under equilibrium and nonequilibrium conditions. *Acc. Chem. Res.* **2019**, *52*, 1006−1015.

(4) Bera, M. K.; Bu, W.; Uysal, A. Liquid Surface X-Ray Scattering. In *Physical Chemistry of Gas-Liquid Interfaces*; Elsevier: 2018; pp 167−194.

(5) Lu, H.; Huang, Y.-C.; Hunger, J.; Gebauer, D.; Cölfen, H.; Bonn, M. Role of Water in CaCO3 Biomineralization. *J. Am. Chem. Soc.* **2021**, *143*, 1758−1762.

(6) Yan, E. C.; Fu, L.; Wang, Z.; Liu, W. Biological macromolecules at interfaces probed by chiral vibrational sum frequency generation spectroscopy. *Chem. Rev.* **2014**, *114*, 8471−8498.

(7) Liang, Z.; Bu, W.; Schweighofer, K. J.; Walwark, D. J.; Harvey, J. S.; Hanlon, G. R.; Amoanu, D.; Erol, C.; Benjamin, I.; Schlossman, M. L. Nanoscale view of assisted ion transport across the liquid−liquid interface. *Proc. Natl. Acad. Sci. U. S. A.* **2019**, *116*, 18227−18232.

(8) Chowdhury, A. U.; Lin, L.; Doughty, B. Hydrogen-Bond-Driven Chemical Separations: Elucidating the Interfacial Steps of Self-Assembly in Solvent Extraction. *ACS Appl. Mater. Interfaces* **2020**, *12*, 32119−32130.

(9) Nayak, S.; Kumal, R. R.; Liu, Z.; Qiao, B.; Clark, A.; Uysal, A. Origins of Clustering of Metalate-Extractant Complexes in Liquid-Liquid Extraction. *ACS Appl. Mater. Interfaces* **2021**, *13*, 24194−24206.

(10) Miller, M.; Liang, Y.; Li, H.; Chu, M.; Yoo, S.; Bu, W.; Olvera de la Cruz, M.; Dutta, P. Electrostatic origin of element selectivity during rare earth adsorption. *Phys. Rev. Lett.* **2019**, *122*, 058001−058001.

(11) Kusaka, R.; Watanabe, M. Mechanism of phase transfer of uranyl ions: a vibrational sum frequency generation spectroscopy study on solvent extraction in nuclear reprocessing. *Phys. Chem. Chem. Phys.* **2018**, *20*, 29588−29590.

(12) Scoppola, E.; Watkins, E. B.; Campbell, R. A.; Konovalov, O.; Girard, L.; Dufrêche, J. F.; Ferru, G.; Fragneto, G.; Diat, O. Solvent extraction: Structure of the liquid−liquid interface containing a diamide ligand. *Angew. Chem.* **2016**, *128*, 9472−9476.

(13) Sun, P.; Huang, K.; Liu, H. Specific Salt Effect on the Interaction between Rare Earth Ions and Trioctylphosphine Oxide Molecules at the Organic−Aqueous Two-Phase Interface: Experi-

ments and Molecular Dynamics Simulations. *Langmuir* **2018**, *34*, 11374−11383.
(14) Fenter, P.; Lee, S. S. Hydration layer structure at solid−water interfaces. *MRS Bull.* **2014**, *39*, 1056−1061.
(15) Johnson, C. M.; Baldelli, S. Vibrational sum frequency spectroscopy studies of the influence of solutes and phospholipids at vapor/water interfaces relevant to biological and environmental systems. *Chem. Rev.* **2014**, *114*, 8416−8446.
(16) Grooms, A. J.; Neal, J. F.; Ng, K. C.; Zhao, W.; Flood, A. H.; Allen, H. C. Thermodynamic Signatures of the Origin of Anti-Hofmeister Selectivity for Phosphate at Aqueous Interfaces. *J. Phys. Chem. A* **2020**, *124*, 5621−5630.
(17) Fumagalli, L.; Esfandiar, A.; Fabregas, R.; Hu, S.; Ares, P.; Janardanan, A.; Yang, Q.; Radha, B.; Taniguchi, T.; Watanabe, K.; Gomila, G.; Novoselov, K. S.; Geim, A. K. Anomalously low dielectric constant of confined water. *Science* **2018**, *360*, 1339−1342.
(18) Bera, M. K.; Antonio, M. R. Polynuclear Speciation of Trivalent Cations near the Surface of an Electrolyte Solution. *Langmuir* **2015**, *31*, 5432−5439.
(19) Jungwirth, P.; Cremer, P. S. Beyond hofmeister. *Nat. Chem.* **2014**, *6*, 261−263.
(20) Leontidis, E. Investigations of the Hofmeister series and other specific ion effects using lipid model systems. *Adv. Colloid Interface Sci.* **2017**, *243*, 8−22.
(21) Kumal, R. R.; Nguyenhuu, H.; Winter, J. E.; McCarley, R. L.; Haber, L. H. Impacts of salt, buffer, and lipid nature on molecular adsorption and transport in liposomes as observed by second harmonic generation. *J. Phys. Chem. C* **2017**, *121*, 15851−15860.
(22) Lovering, K.; Nayak, S.; Bu, W.; Uysal, A. The Role of Specific Ion Effects in Ion Transport: The Case of Nitrate and Thiocyanate. *J. Phys. Chem. C* **2020**, *124*, 573−581.
(23) Nayak, S.; Lovering, K.; Uysal, A. Ion-Specific Clustering of Metal-Amphiphile Complexes in Rare Earth Separations. *Nanoscale* **2020**, *12*, 20202−20210.
(24) Millefiori, S.; Foffani, A. Dipole moments and rotational isomerism for organic thio-and selenocyanates. *Tetrahedron* **1966**, *22*, 803−811.
(25) Viswanath, P.; Motschmann, H. Oriented thiocyanate anions at the air− electrolyte interface and its implications on interfacial water-a vibrational sum frequency spectroscopy study. *J. Phys. Chem. C* **2007**, *111*, 4484−4486.
(26) Tesei, G.; Aspelin, V.; Lund, M. Specific Cation Effects on SCN−in Bulk Solution and at the Air−Water Interface. *J. Phys. Chem. B* **2018**, *122*, 5094−5105.
(27) Viswanath, P.; Aroti, A.; Motschmann, H.; Leontidis, E. Vibrational Sum Frequency Generation Spectroscopic Investigation of the Interaction of Thiocyanate Ions with Zwitterionic Phospholipid Monolayers at the Air− Water Interface. *J. Phys. Chem. B* **2009**, *113*, 14816−14823.
(28) Viswanath, P.; Motschmann, H. Effect of interfacial presence of oriented thiocyanate on water structure. *J. Phys. Chem. C* **2008**, *112*, 2099−2103.
(29) Hao, H.; Xie, Q.; Ai, J.; Wang, Y.; Bian, H. Specific counter-cation effect on the molecular orientation of thiocyanate anions at the aqueous solution interface. *Phys. Chem. Chem. Phys.* **2020**, *22*, 10106−10115.
(30) Mizuno, H.; Rizzuto, A. M.; Saykally, R. J. Charge-Transfer-to-Solvent Spectrum of Thiocyanate at the Air/Water Interface Measured by Broadband Deep Ultraviolet Electronic Sum Frequency Generation Spectroscopy. *J. Phys. Chem. Lett.* **2018**, *9*, 4753−4757.
(31) Onorato, R. M.; Otten, D. E.; Saykally, R. J. Adsorption of thiocyanate ions to the dodecanol/water interface characterized by UV second harmonic generation. *Proc. Natl. Acad. Sci. U. S. A.* **2009**, *106*, 15176−15180.
(32) Schultz, P. W.; Leroi, G. E.; Popov, A. I. Solvation of SCN-and SeCN-anions in hydrogen-bonding solvents. *J. Am. Chem. Soc.* **1996**, *118*, 10617−10625.
(33) Lenchenkov, V.; She, C.; Lian, T. Vibrational relaxation of cn stretch of pseudo-halide anions (OCN-, SCN-, and SeCN-) in polar solvents. *J. Phys. Chem. B* **2006**, *110*, 19990−19997.
(34) Yuan, R.; Yan, C.; Tamimi, A.; Fayer, M. D. Molecular anion hydrogen bonding dynamics in aqueous solution. *J. Phys. Chem. B* **2015**, *119*, 13407−13415.
(35) Lindquist, B. A.; Corcelli, S. A. Nitrile Groups as Vibrational Probes: Calculations of the C-N Infrared Absorption Line Shape of Acetonitrile in Water and Tetrahydrofuran. *J. Phys. Chem. B* **2008**, *112*, 6301−6303.
(36) Piontek, S. M.; DelloStritto, M.; Mandal, B.; Marshall, T.; Klein, M. L.; Borguet, E. Probing Heterogeneous Charge Distributions at the α-Al2O3 (0001)/H_2O Interface. *J. Am. Chem. Soc.* **2020**, *142* (28), 12096−12105.
(37) Patrow, J. G.; Sorenson, S. A.; Dawlaty, J. M. Direct spectroscopic measurement of interfacial electric fields near an electrode under polarizing or current-carrying conditions. *J. Phys. Chem. C* **2017**, *121*, 11585−11592.
(38) Ge, A.; Videla, P. E.; Lee, G. L.; Rudshteyn, B.; Song, J.; Kubiak, C. P.; Batista, V. S.; Lian, T. Interfacial structure and electric field probed by in situ electrochemical vibrational Stark effect spectroscopy and computational modeling. *J. Phys. Chem. C* **2017**, *121*, 18674−18682.
(39) Karmakar, A.; Duvail, M.; Bley, M.; Zemb, T.; Dufrêche, J.-F. Combined supramolecular and mesoscale modelling of liquid−liquid extraction of rare earth salts. *Colloids Surf, A Physicochem Eng. Asp* **2018**, *555*, 713−727.
(40) Preez, A. d.; S Preston, J. The solvent extraction of rare-earth metals by carboxylic acids. *Solvent Extr. Ion Exch.* **1992**, *10*, 207−230.
(41) Nayak, S.; Lovering, K. A.; Bu, W.; Uysal, A. Anions Enhance Rare Earth Adsorption at Negatively Charged Surfaces. *J. Phys. Chem. Lett.* **2020**, *11*, 4436−4442.
(42) Gradzielski, M.; Duvail, M.; de Molina, P. M.; Simon, M.; Talmon, Y.; Zemb, T. Using Microemulsions: Formulation Based on Knowledge of Their Mesostructure. *Chem. Rev.* **2021**, *121*, 5671−5740.
(43) Wang, J.; Arrachart, G.; Giusti, F.; Martin-Gassin, G.; Gassin, P.-M.; Jonchere, A.; Diat, O.; Girard, L. Synthesis and Characterization of a Chromo-Extractant to the Probe Liquid−Liquid Interface in a Solvent Extraction Process. *J. Phys. Chem. C* **2020**, *124*, 10916−10923.
(44) Chen, X.; Hua, W.; Huang, Z.; Allen, H. C. Interfacial water structure associated with phospholipid membranes studied by phase-sensitive vibrational sum frequency generation spectroscopy. *J. Am. Chem. Soc.* **2010**, *132*, 11336−11342.
(45) Mondal, J. A.; Nihonyanagi, S.; Yamaguchi, S.; Tahara, T. Three distinct water structures at a zwitterionic lipid/water interface revealed by heterodyne-detected vibrational sum frequency generation. *J. Am. Chem. Soc.* **2012**, *134*, 7842−7850.
(46) Sthoer, A.; Tyrode, E. Interactions of Na+ cations with a highly charged fatty acid langmuir monolayer: molecular description of the phase transition. *J. Phys. Chem. C* **2019**, *123*, 23037−23048.
(47) Sung, W.; Krem, S.; Kim, D. Binding of trivalent ions on fatty acid Langmuir monolayer: Fe3+ versus La3+. *J. Chem. Phys.* **2018**, *149*, 163304−163307.
(48) Yan, C.; Thomaz, J. E.; Wang, Y.-L.; Nishida, J.; Yuan, R.; Breen, J. P.; Fayer, M. D. Ultrafast to ultraslow dynamics of a Langmuir monolayer at the air/water interface observed with reflection enhanced 2D IR spectroscopy. *J. Am. Chem. Soc.* **2017**, *139*, 16518−16527.
(49) Uysal, A.; Chu, M.; Stripe, B.; Timalsina, A.; Chattopadhyay, S.; Schlepütz, C. M.; Marks, T. J.; Dutta, P. What x rays can tell us about the interfacial profile of water near hydrophobic surfaces. *Phys. Rev. B* **2013**, *88*, 035431−035438.
(50) Zdrali, E.; Okur, H. I.; Roke, S. Specific ion effects at the interface of nanometer-sized droplets in water: structure and stability. *J. Phys. Chem. C* **2019**, *123*, 16621−16630.
(51) Hamal, P.; Nguyenhuu, H.; Subasinghege Don, V.; Kumal, R. R.; Kumar, R.; McCarley, R. L.; Haber, L. H. Molecular adsorption

and transport at liposome surfaces studied by molecular dynamics simulations and second harmonic generation spectroscopy. *J. Phys. Chem. B* **2019**, *123*, 7722−7730.
(52) Hamal, P. *Second Harmonic Generation Spectroscopy and Microscopy of Liposomes, Nanoparticles, and Cells* **2020**.
(53) Eisenthal, K. Liquid interfaces probed by second-harmonic and sum-frequency spectroscopy. *Chem. Rev.* **1996**, *96*, 1343−1360.
(54) Geiger, F. M. Second harmonic generation, sum frequency generation, and χ (3): dissecting environmental interfaces with a nonlinear optical Swiss Army knife. *Annu. Rev. Phys. Chem.* **2009**, *60*, 61−83.
(55) Horowitz, Y.; Steinruck, H.-G.; Han, H.-L.; Cao, C.; Abate, I. I.; Tsao, Y.; Toney, M. F.; Somorjai, G. A. Fluoroethylene carbonate induces ordered electrolyte interface on silicon and sapphire surfaces as revealed by sum frequency generation vibrational spectroscopy and X-ray reflectivity. *Nano Lett.* **2018**, *18*, 2105−2111.
(56) Sung, W.; Wang, W.; Lee, J.; Vaknin, D.; Kim, D. Specificity and variation of length scale over which monovalent halide ions neutralize a charged interface. *J. Phys. Chem. C* **2015**, *119*, 7130−7137.
(57) Nojima, Y.; Suzuki, Y.; Yamaguchi, S. Weakly hydrogen-bonded water inside charged lipid monolayer observed with heterodyne-detected vibrational sum frequency generation spectroscopy. *J. Phys. Chem. C* **2017**, *121*, 2173−2180.
(58) Mondal, J. A.; Nihonyanagi, S.; Yamaguchi, S.; Tahara, T. Structure and orientation of water at charged lipid monolayer/water interfaces probed by heterodyne-detected vibrational sum frequency generation spectroscopy. *J. Am. Chem. Soc.* **2010**, *132*, 10656−10657.
(59) Krem, S.; Lee, M.; Sam, S.; Sung, W.; Kim, D. Structure of Electric Double Layer under Cationic Langmuir Monolayer: Charge Condensation Effect. *J. Phys. Chem. Lett.* **2021**, *12*, 3417−3423.
(60) Sung, W.; Kim, D.; Shen, Y. Sum-frequency vibrational spectroscopic studies of Langmuir monolayers. *Curr. Appl. Phys.* **2013**, *13*, 619−632.
(61) Rao, Y.; Tao, Y.-s.; Wang, H.-f. Quantitative analysis of orientational order in the molecular monolayer by surface second harmonic generation. *J. Chem. Phys.* **2003**, *119*, 5226−5236.
(62) Uysal, A.; Rock, W.; Qiao, B.; Bu, W.; Lin, B. Two-Step Adsorption of PtCl62−Complexes at a Charged Langmuir Monolayer: Role of Hydration and Ion Correlations. *J. Phys. Chem. C* **2017**, *121*, 25377−25383.
(63) Bu, W.; Vaknin, D. X-ray fluorescence spectroscopy from ions at charged vapor/water interfaces. *J. Appl. Phys.* **2009**, *105*, 084911.
(64) Bu, W.; Hou, B.; Mihaylov, M.; Kuzmenko, I.; Lin, B.; Meron, M.; Soderholm, L.; Luo, G.; Schlossman, M. L. X-ray fluorescence from a model liquid/liquid solvent extraction system. *J. Appl. Phys.* **2011**, *110*, 102214−102216.
(65) Bu, W.; Mihaylov, M.; Amoanu, D.; Lin, B.; Meron, M.; Kuzmenko, I.; Soderholm, L.; Schlossman, M. L. X-ray studies of interfacial strontium−extractant complexes in a model solvent extraction system. *J. Phys. Chem. B* **2014**, *118*, 12486−12500.
(66) Rock, W.; Qiao, B.; Zhou, T.; Clark, A. E.; Uysal, A. Heavy Anionic Complex Creates a Unique Water Structure at a Soft Charged Interface. *J. Phys. Chem. C* **2018**, *122*, 29228−29236.
(67) Ishiyama, T.; Imamura, T.; Morita, A. Theoretical studies of structures and vibrational sum frequency generation spectra at aqueous interfaces. *Chem. Rev.* **2014**, *114*, 8447−8470.
(68) Zhang, Z.; Kim, J.; Khoury, R.; Saghayezhian, M.; Haber, L. H.; Plummer, E. Surface sum frequency generation spectroscopy on non-centrosymmetric crystal GaAs (001). *Surf. Sci.* **2017**, *664*, 21−28.
(69) Zhuang, X.; Miranda, P.; Kim, D.; Shen, Y. Mapping molecular orientation and conformation at interfaces by surface nonlinear optics. *Phys. Rev. B* **1999**, *59*, 12632−12640.
(70) Verreault, D.; Hua, W.; Allen, H. C. From conventional to phase-sensitive vibrational sum frequency generation spectroscopy: probing water organization at aqueous interfaces. *J. Phys. Chem. Lett.* **2012**, *3*, 3012−3028.
(71) Lambert, A. G.; Davies, P. B.; Neivandt, D. J. Implementing the theory of sum frequency generation vibrational spectroscopy: a tutorial review. *Appl. Spectrosc. Rev.* **2005**, *40*, 103−145.
(72) Stiopkin, I. V.; Jayathilake, H. D.; Bordenyuk, A. N.; Benderskii, A. V. Heterodyne-detected vibrational sum frequency generation spectroscopy. *J. Am. Chem. Soc.* **2008**, *130*, 2271−2275.
(73) Ohno, P. E.; Wang, H.-f.; Geiger, F. M. Second-order spectral lineshapes from charged interfaces. *Nat. Commun.* **2017**, *8*, 1−9.
(74) Wen, Y.-C.; Zha, S.; Liu, X.; Yang, S.; Guo, P.; Shi, G.; Fang, H.; Shen, Y. R.; Tian, C. Unveiling microscopic structures of charged water interfaces by surface-specific vibrational spectroscopy. *Phys. Rev. Lett.* **2016**, *116*, 016101−016105.
(75) Ma, E.; Kim, J.; Chang, H.; Ohno, P. E.; Jodts, R. J.; Miller, T. F., III; Geiger, F. M. Stern and Diffuse Layer Interactions During Ionic Strength Cycling. *J. Phys. Chem. C* **2021**, *125*, 18002−18014.
(76) Ohno, P. E.; Saslow, S. A.; Wang, H.-f.; Geiger, F. M.; Eisenthal, K. B. Phase-referenced nonlinear spectroscopy of the α-quartz/water interface. *Nat. Commun.* **2016**, *7*, 1−5.
(77) Montenegro, A.; Dutta, C.; Mammetkuliev, M.; Shi, H.; Hou, B.; Bhattacharyya, D.; Zhao, B.; Cronin, S. B.; Benderskii, A. V. Asymmetric response of interfacial water to applied electric fields. *Nature* **2021**, *594*, 62−65.
(78) Ma, E.; Ohno, P. E.; Kim, J.; Liu, Y.; Lozier, E. H.; Miller, T. F., III; Wang, H.-F.; Geiger, F. M. A New Imaginary Term in the Second-Order Nonlinear Susceptibility from Charged Interfaces. *J. Phys. Chem. Lett.* **2021**, *12*, 5649−5659.
(79) Wang, H.-F. Sum frequency generation vibrational spectroscopy (SFG-VS) for complex molecular surfaces and interfaces: Spectral lineshape measurement and analysis plus some controversial issues. *Prog. Surf. Sci.* **2016**, *91*, 155−182.
(80) Málková, Š.; Long, F.; Stahelin, R. V.; Pingali, S. V.; Murray, D.; Cho, W.; Schlossman, M. L. X-ray reflectivity studies of cPLA2α-C2 domains adsorbed onto Langmuir monolayers of SOPC. *Biophys. J.* **2005**, *89*, 1861−1873.
(81) Bu, W.; Yu, H.; Luo, G.; Bera, M. K.; Hou, B.; Schuman, A. W.; Lin, B.; Meron, M.; Kuzmenko, I.; Antonio, M. R.; Soderholm, L.; Schlossman, M. L. Observation of a rare earth ion−extractant complex arrested at the oil−water interface during solvent extraction. *J. Phys. Chem. B* **2014**, *118*, 10662−10674.
(82) Altman, R. M.; Richmond, G. L. Coming to Order: Adsorption and Structure of Nonionic Polymer at the Oil/Water Interface as Influenced by Cationic and Anionic Surfactants. *Langmuir* **2020**, *36*, 1975−1984.
(83) Danauskas, S. M.; Li, D.; Meron, M.; Lin, B.; Lee, K. Y. C. Stochastic fitting of specular X-ray reflectivity data using StochFit. *J. Appl. Crystallogr.* **2008**, *41*, 1187−1193.
(84) Rock, W.; Oruc, M. E.; Ellis, R. J.; Uysal, A. Molecular scale description of anion competition on amine-functionalized surfaces. *Langmuir* **2016**, *32*, 11532−11539.
(85) Tuladhar, A.; Piontek, S. M.; Frazer, L.; Borguet, E. Effect of halide anions on the structure and dynamics of water next to an alumina (0001) surface. *J. Phys. Chem. C* **2018**, *122* (24), 12819−12830.
(86) Jena, K. C.; Covert, P. A.; Hore, D. K. The effect of salt on the water structure at a charged solid surface: Differentiating second-and third-order nonlinear contributions. *J. Phys. Chem. Lett.* **2011**, *2*, 1056−1061.
(87) Kumal, R. R. Nanoparticle-Based Drug-Delivery Systems Studied by Second Harmonic Generation. Ph.D. Dissertation, Louisiana State University, Baton Rouge, LA, 2017.
(88) Rehl, B.; Gibbs, J. M. Role of Ions on the Surface-Bound Water Structure at the Silica/Water Interface: Identifying the Spectral Signature of Stability. *J. Phys. Chem. Lett.* **2021**, *12*, 2854−2864.
(89) Kumal, R. R.; Karam, T. E.; Haber, L. H. Determination of the surface charge density of colloidal gold nanoparticles using second harmonic generation. *J. Phys. Chem. C* **2015**, *119*, 16200−16207.
(90) Tarbuck, T. L.; Richmond, G. L. Adsorption and Reaction of CO_2 and SO2 at a Water Surface. *J. Am. Chem.* **2006**, *128*, 3256−3267.

https://doi.org/10.1021/acs.jpcc.1c06925
J. Phys. Chem. C 2022, 126, 1140−1151

(91) Allen, H. C.; Casillas-Ituarte, N. N.; Sierra-Hernandez, M. R.; Chen, X.; Tang, C. Y. Shedding light on water structure at air−aqueous interfaces: ions, lipids, and hydration. *Phys. Chem. Chem. Phys.* **2009**, *11*, 5538−5549.
(92) Covert, P. A.; Jena, K. C.; Hore, D. K. Throwing salt into the mix: Altering interfacial water structure by electrolyte addition. *J. Phys. Chem. Lett.* **2014**, *5*, 143−148.

https://doi.org/10.1021/acs.jpcc.1c06925
J. Phys. Chem. C 2022, 126, 1140−1151